Comput Geosci (2016) 20:1169–1184
DOI 10.1007/s10596-016-9583-2

ORIGINAL PAPER

A semi-implicit method for incompressible three-phase flow in porous media

Justin Dong[1] · **Béatrice Rivière**[1]

Received: 15 June 2015 / Accepted: 30 June 2016 / Published online: 12 August 2016

Abstract In this paper, we present a semi-implicit method for the incompressible three-phase flow equations in two dimensions. In particular, a high-order discontinuous Galerkin spatial discretization is coupled with a backward Euler discretization in time. We consider a pressure-saturation formulation, decouple the pressure and saturation equations, and solve them sequentially while still keeping each equation implicit in its respective unknown. We present several numerical examples on both homogeneous and heterogeneous media, with varying permeability and porosity. Our results demonstrate the robustness of the scheme. In particular, no slope limiters are required and a relatively large time step may be taken.

Keywords Semi-implicit · Discontinuous Galerkin · High order · Heterogeneous permeability and porosity

1 Introduction

Many flow systems in porous media can be categorized as a three-phase flow, such as light oil, heavy oil, and water. Predicting the evolution of the phases in space and time is essential in the decision-making process for the oil and gas industry. The mathematical models are based on mass conservation laws for each phase. Two-phase flow models have been heavily studied in the literature, and there exist many approximations of capillary pressure and relative permeabilities that are validated by core-flooding experiments [8]. On one hand, three-phase flow models can be viewed as an extension of the two-phase flow models. On the other hand, there is less consensus on the appropriate choice of the capillary pressure and relative permeability curves and existing models from two-phase data may not agree with experimental results [3].

Our paper applies a discontinuous Galerkin (DG) method that uses piecewise polynomials of degree from one to four to solve the incompressible three-phase flow problem. DG methods have been successfully applied to single-phase flow [5, 14] and to two-phase flow [13, 15, 16]. In particular, robustness of the methods for single-phase and two-phase flow in heterogeneous media was shown in [4, 17]. The lack of continuity between the mesh elements makes the DG method very suitable for flow and transport in porous media. Local mass conservation is an inherent property of the DG method. In addition, the method allows for discontinuous input data if discontinuity lines agree with the mesh skeleton. Any promising discretization of the three-phase flow problem should handle the strong heterogeneities of the medium. In this paper, we use realistic values for the permeability and porosity fields. We note that the permeability values usually vary across six orders of magnitude. These variations yield highly varying phase velocities via the generalized Darcy's law. Popular methods used by the oil and gas industry are the finite difference methods and the

Both authors acknowledge the support of the National Science Foundation grant NSF-DMS 1318348.

✉ Béatrice Rivière
riviere@rice.edu

Justin Dong
justin.dong@alumni.rice.edu

[1] Computational and Applied Mathematics Department, Rice University, Houston, TX, USA

cell-centered finite volume methods. Both methods are only of first order and exhibit numerical diffusion, particularly in the case of heterogeneities [2, 18]. Other methods for solving the three-phase problem include mixed finite elements and streamline front tracking [1, 7, 9].

In a three-phase model, the unknowns, which are the saturation and pressure for each phase, are related through relations like capillary pressures. This results in three independent unknowns. In our work, we solve for the heavy oil pressure and the water and light oil saturations. We show convergence of the method for discontinuous input data, such as permeability and porosity fields. We vary the polynomial degree between one and four. This paper is related to a previous work for modeling three-phase flow in homogeneous one-dimensional domains [12]. In a recent paper, the DG method was applied to solve the black-oil problem in one-dimensional domains, which is a compressible three-phase flow. In addition, the gas phase is assumed to be miscible in the oil phase [20]. In [19], the finite volume method is combined with a DG method and slope limiters to solve the two-phase and three-phase flow problems in the absence of capillary pressure.

An outline of the paper follows. In the next section, we introduce the saturation and pressure equations and the input data. The numerical scheme is described in Section 4. Simulations on homogeneous and heterogeneous porous media are shown in Section 5. Conclusions follow.

2 The model problem

For a porous medium $\Omega \subseteq \mathbb{R}^2$, the incompressible three-phase flow formulation consists of a coupled system of three nonlinear partial differential equations. We denote the phases by liquid (heavy oil), aqueous (water), and vapor (light oil) and derive a pressure-saturation formulation using the pressure of the liquid phase. The pressure of the liquid phase is denoted by p_{o} and the saturations of the aqueous and vapor phases are denoted by s_{w} and s_{g}, respectively. We have:

$$\begin{aligned}\frac{\partial(\phi s_{\mathrm{w}})}{\partial t} &+ \nabla\cdot\frac{\lambda_{\mathrm{w}}}{\lambda_{\mathrm{t}}}\left(\mathbf{u}+K\lambda_{\mathrm{g}}p'_{\mathrm{cgo}}\nabla s_{\mathrm{w}}\right)\\ &- \nabla\cdot\left(K\frac{\lambda_{\mathrm{w}}(\lambda_{\mathrm{o}}+\lambda_{\mathrm{g}})}{\lambda_{\mathrm{t}}}p'_{\mathrm{cwo}}\nabla s_{\mathrm{w}}\right)\\ &= 0\end{aligned} \tag{1}$$

$$\begin{aligned}\frac{\partial(\phi s_{\mathrm{g}})}{\partial t} &+ \nabla\cdot\frac{\lambda_{\mathrm{g}}}{\lambda_{\mathrm{t}}}\left(\mathbf{u}+K\lambda_{\mathrm{w}}p'_{\mathrm{cwo}}\nabla s_{\mathrm{g}}\right)\\ &- \nabla\cdot\left(K\frac{\lambda_{\mathrm{g}}(\lambda_{\mathrm{o}}+\lambda_{\mathrm{w}})}{\lambda_{\mathrm{t}}}p'_{\mathrm{cgo}}\nabla s_{\mathrm{g}}\right)\\ &= 0\end{aligned} \tag{2}$$

and

$$\nabla\cdot\mathbf{u} = 0 \tag{3}$$

$$\begin{aligned}\mathbf{u} = &-K\lambda_{\mathrm{t}}\nabla p_{\mathrm{o}} - K\lambda_{\mathrm{w}}p'_{\mathrm{cwo}}\nabla s_{\mathrm{w}}\\ &-K\lambda_{\mathrm{g}}p'_{\mathrm{cgo}}\nabla s_{\mathrm{g}}\end{aligned} \tag{4}$$

Here, $\mathbf{u}$ denotes the total velocity of the system. The porosity and permeability of the medium are denoted by ϕ and K, respectively. The phase mobilities are denoted by λ_α for $\alpha \in \{w, o, g\}$ with the notion that the total mobility λ_{t} is given by $\lambda_{\mathrm{t}} = \lambda_{\mathrm{w}} + \lambda_{\mathrm{o}} + \lambda_{\mathrm{g}}$. The aqueous and vapor phase mobilities are functions of their respective saturations and viscosities, while the liquid phase mobility is a function of both the aqueous and vapor saturations and viscosities. In this paper, the order of wettability is water, heavy oil, and light oil and we take the following phase mobilities [22]:

$$\begin{aligned}&\lambda_{\mathrm{w}}(s_{\mathrm{w}}) = \tfrac{s_{\mathrm{w}}^2}{\mu_{\mathrm{w}}}, \quad \lambda_{\mathrm{g}}(s_{\mathrm{g}}) = \tfrac{s_{\mathrm{g}}^2}{\mu_{\mathrm{g}}}\\ &\lambda_{\mathrm{o}}(s_{\mathrm{w}}, s_{\mathrm{g}}) = \tfrac{(1-s_{\mathrm{w}}-s_{\mathrm{g}})(1-s_{\mathrm{w}})(1-s_{\mathrm{g}})}{\mu_{\mathrm{o}}}\end{aligned} \tag{5}$$

The difference between the phase pressures are the capillary pressures and they are denoted by p_{cwp} and p_{cgo}: $p_{\mathrm{cwo}} = p_{\mathrm{o}} - p_{\mathrm{w}}$ and $p_{\mathrm{cgo}} = p_{\mathrm{g}} - p_{\mathrm{o}}$. Using the notion that these capillary pressures are positive and decreasing, we see that $p'_{\mathrm{cwo}} < 0$ and $p'_{\mathrm{cgo}} < 0$. We consider the following model of capillary pressures [6, 10]:

$$p_{\mathrm{cwo}} = \frac{913.6890}{\ln\left(\frac{0.01}{1-s_{\mathrm{wr}}}\right)}\ln\left(\frac{s_{\mathrm{w}}-s_{\mathrm{wr}}+0.01}{1-s_{\mathrm{wr}}}\right) \tag{6}$$

$$\begin{aligned}p_{\mathrm{cgo}} = &\frac{565.617}{\ln\left(\frac{0.01}{1-s_{\mathrm{wr}}-s_{\mathrm{or}}}\right)}\\ &\times\ln\left(\frac{1.01-s_{\mathrm{g}}-s_{\mathrm{wr}}-s_{\mathrm{or}}}{1-s_{\mathrm{wr}}-s_{\mathrm{or}}}\right)\end{aligned} \tag{7}$$

Here, the residual saturations are denoted by $s_{\alpha r}$. For the boundary conditions, we partition $\partial\Omega$ into several disjoint sets, namely $\partial\Omega = \Gamma_{p_1}\cup\Gamma_{p_2} = \Gamma_{s_1}\cup\Gamma_{s_2}$. On the boundaries Γ_{p_1} and Γ_{s_1}, we have Dirichlet boundary conditions and on Γ_{p_2} and Γ_{s_2}, we have no-flow (zero Neumann) boundary conditions. For the pressure equation, we have:

$$p_{\mathrm{o}} = p_{\mathrm{o,D}}, \quad \text{on } \Gamma_{p_1} \tag{8}$$

$$K\lambda_{\mathrm{t}}\nabla p_{\mathrm{o}}\cdot\mathbf{n}_e = 0, \quad \text{on } \Gamma_{p_2} \tag{9}$$

For the saturation equations, we have:

$$s_{\mathrm{w}} = s_{\mathrm{w,D}}, \quad \text{on } \Gamma_{s_1} \tag{10}$$

$$K\tfrac{\lambda_{\mathrm{w}}(\lambda_{\mathrm{o}}+\lambda_{\mathrm{g}})}{\lambda_{\mathrm{t}}}p'_{\mathrm{cwo}}\nabla s_{\mathrm{w}}\cdot\mathbf{n}_e = 0, \quad \text{on } \Gamma_{s_2} \tag{11}$$

and

$$s_{\mathrm{g}} = s_{\mathrm{g,D}}, \quad \text{on } \Gamma_{s_1} \tag{12}$$

$$K\tfrac{\lambda_{\mathrm{g}}(\lambda_{\mathrm{o}}+\lambda_{\mathrm{w}})}{\lambda_{\mathrm{t}}}p'_{\mathrm{cgo}}\nabla s_{\mathrm{g}}\cdot\mathbf{n}_e = 0, \quad \text{on } \Gamma_{s_2} \tag{13}$$

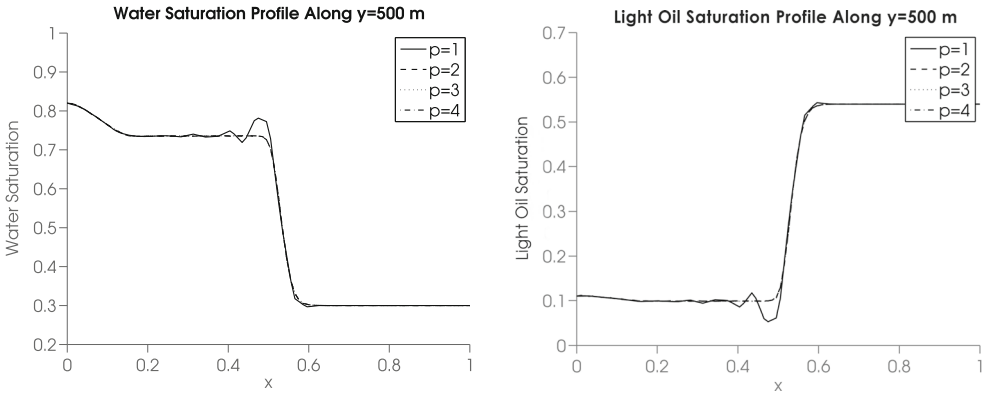

Fig. 1 A comparison of the saturation profiles for $p \in \{1, 2, 3, 4\}$ after 100 days

3 Variational formulation

We consider a partitioning $\mathcal{M}_h$ of the computational domain Ω into triangular elements. Furthermore, we indicate the set of interior edges of $\mathcal{M}_h$ by Γ_h^i. We define the subspace of discontinuous polynomial basis functions as

$$\mathcal{V} = \left\{ v : v|_T \in \mathbb{P}_p(T),\, p \geqslant 1,\, T \in \mathcal{M}_h \right\}$$

Here, $\mathbb{P}_p(T)$ is the space of all polynomials of degree p defined on the triangular element T.

For a given edge $e \in \Gamma_h^i$, we denote its element neighbors by T_1 and T_2 using the convention that T_1 is the element with the lower global number. Furthermore, we define $\mathbf{n}_e$ to be the unit normal vector that points from T_1 to T_2. If $e \in \partial\Omega$, then we use the convention that $\mathbf{n}_e$ points outward. For the DG variational formulation, we define the jump $[\cdot]$ and average $\langle\cdot\rangle$ of a function v along an edge e:

$$[v] = v|_{T_1} - v|_{T_2}$$
$$\langle v \rangle = \tfrac{1}{2}\left(v|_{T_1} + v|_{T_2}\right)$$

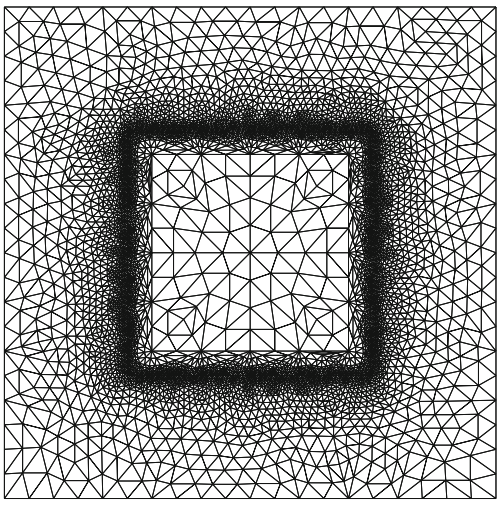

Fig. 2 The refined mesh for the second example of an inhomogeneous medium with $\Omega_K = [250\text{ m}, 750\text{ m}]^2$

3.1 The heavy oil pressure equation

We first define the auxiliary variables $\boldsymbol{\zeta} = K\lambda_w p'_{cwo}\nabla s_w$ and $\xi = K\lambda_g p'_{cgo}\nabla s_g$. Then, we can rewrite Eqs. 3 and 4 as follows:

$$-\nabla\cdot(K\lambda_t\nabla p_o) = -\nabla\cdot\boldsymbol{\zeta} - \nabla\cdot\boldsymbol{\xi} \tag{14}$$

We multiply by a test function $v \in \mathcal{V}$ and integrate by parts. Summing over all of the elements in $\mathcal{M}_h$ and edges in $\Gamma_h^i \cup \partial\Omega$, we obtain:

$$\begin{aligned}
\sum_{T\in\mathcal{M}_h} & \int_T K\lambda_t\nabla p_o\cdot\nabla v \\
& - \sum_{e\in\Gamma_h^i\cup\Gamma_{p_1}} \int_e \langle K\lambda_t\nabla p_o\cdot\mathbf{n}_e\rangle[v] \\
& + \epsilon \sum_{e\in\Gamma_h^i\cup\Gamma_{p_1}} \int_e \langle K\lambda_t\nabla v\cdot\mathbf{n}_e\rangle[p_o] \\
& + \sum_{e\in\Gamma_h^i\cup\Gamma_{p_1}} \frac{\sigma}{|e|}\int_e [p_o][v] \\
= & \sum_{T\in\mathcal{M}_h}\int_T \nabla v\cdot\zeta - \sum_{e\in\Gamma_h^i\cup\partial\Omega}\int_e \zeta^*\cdot\mathbf{n}_e[v] \\
& + \sum_{T\in\mathcal{M}_h}\int_T \nabla v\cdot\xi - \sum_{e\in\Gamma_h^i\cup\partial\Omega}\int_e \xi^*\cdot\mathbf{n}_e[v] \\
& + \sum_{e\in\Gamma_{p_1}}\int_e \left(\epsilon K\lambda_t\nabla v\cdot\mathbf{n}_e + \frac{\sigma}{|e|}v\right) p_{o,D}
\end{aligned} \tag{15}$$

Here, $(\cdot)^*$ denotes the numerical upwind flux, defined on a given edge $e \in \Gamma_h^i$ by:

$$\zeta^* = \begin{cases} \zeta|_{T_1}, & \langle\zeta\cdot\mathbf{n}_e\rangle \geqslant 0 \\ \zeta|_{T_2}, & \langle\zeta\cdot\mathbf{n}_e\rangle < 0 \end{cases} \qquad \xi^* = \begin{cases} \xi|_{T_1}, & \langle\xi\cdot\mathbf{n}_e\rangle \geqslant 0 \\ \xi|_{T_2}, & \langle\xi\cdot\mathbf{n}_e\rangle < 0 \end{cases}$$

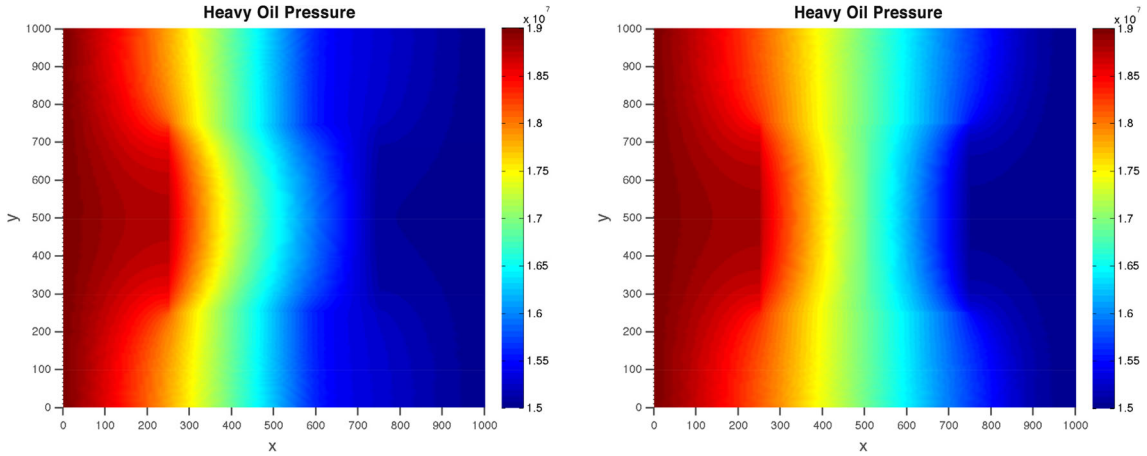

Fig. 3 The two-dimensional pressure contours at 113 (*left*) and 226 (*right*) days for the example on an inhomogeneous medium using NIPG with $\sigma = 1.0$ and $p = 2$

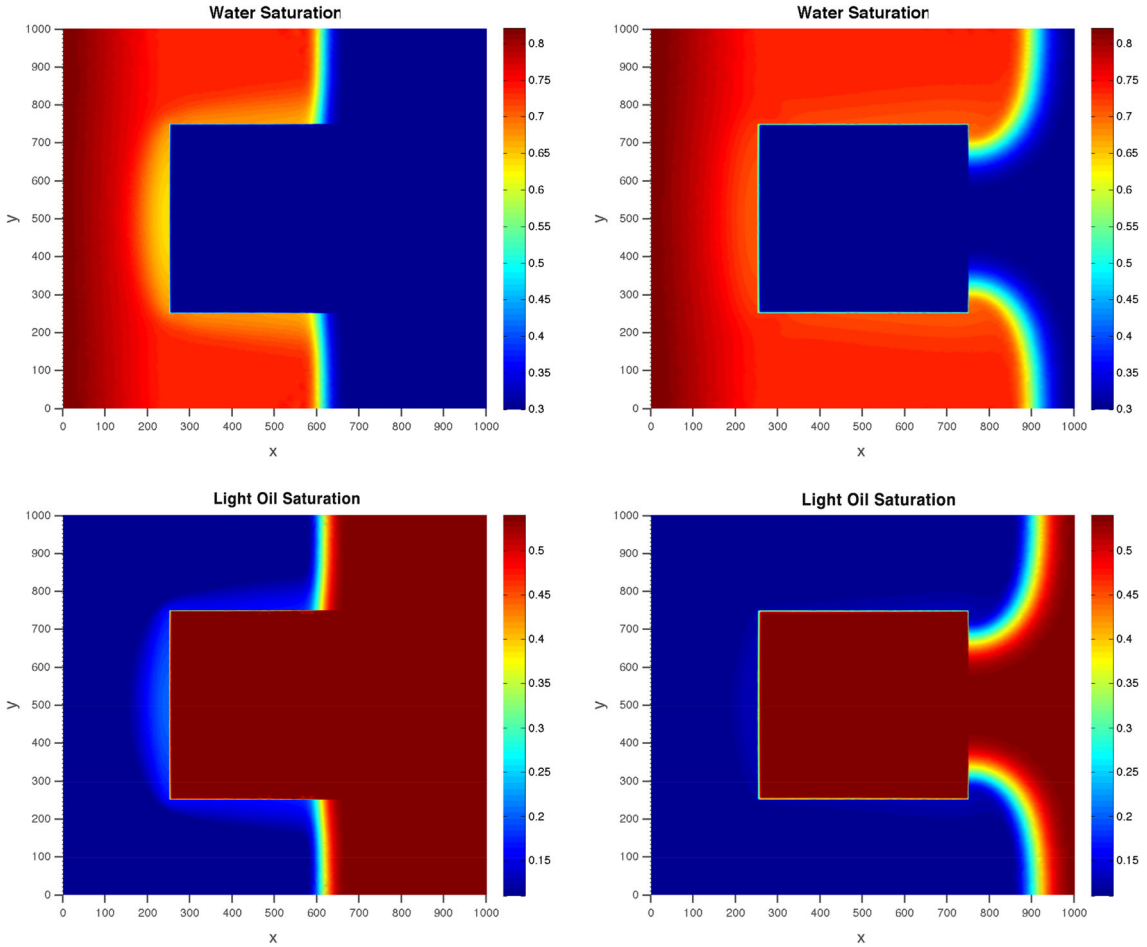

Fig. 4 The two-dimensional saturation contours at 113 (*left*) and 226 (*right*) days for the example on an inhomogeneous medium using NIPG with $\sigma = 1.0$ and $p = 2$

Additionally, ϵ and σ are parameters that differentiate between the variants of the DG method. The penalty term is essential to any DG formulation as it helps enforce continuity between the mesh elements in a weak sense. For $\epsilon = -1$ and $\sigma > 0$, the matrix arising from the discretization of the elliptic operator $-\nabla \cdot K\nabla p_0$ is symmetric and we obtain the symmetric interior penalty Galerkin (SIPG) method. For $\epsilon = 1$ and $\sigma \geqslant 0$, the matrix is non-symmetric and we refer to this choice of parameters as the non-symmetric interior penalty Galerkin (NIPG) method.

For SIPG, the penalty parameter has to be large enough in order to have stability of the method [21]. For the NIPG method, there is no stability restriction on the value of the penalty parameter and it is chosen equal to one. If the polynomial degree of the approximation is greater than or equal to 2, then the penalty term for the NIPG method is not needed for stability. We will allow these penalty parameters to vary in our numerical simulations.

3.2 The water saturation equation

We define the auxiliary variables $\boldsymbol{\chi}$ and α:

$$\begin{aligned}\boldsymbol{\chi}(p_o, s_w, s_g) &= \mathbf{u}(p_o, s_w, s_g) + K\lambda_g p'_{cgo}\nabla s_g \\ \alpha(s_w, s_g) &= \frac{\lambda_w(\lambda_o + \lambda_g)}{\lambda_t} p'_{cwo}\end{aligned}$$

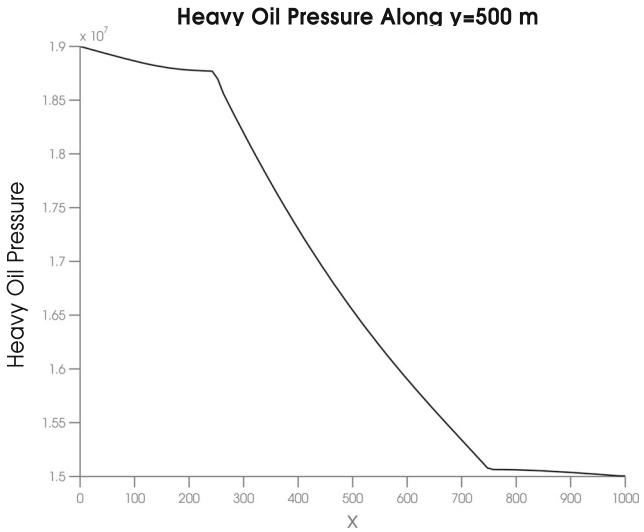

Fig. 5 The pressure profile along $y = 500$ at 113 days for the example on an inhomogeneous medium using NIPG with $\sigma = 1.0$ and $p = 2$

and rewrite (1) as follows:

$$\begin{aligned}\frac{\partial(\phi s_w)}{\partial t} &+ \nabla \cdot \frac{\lambda_w}{\lambda_t}\chi(p_o, s_w, s_g) \\ &- \nabla \cdot \left(K\alpha(s_w, s_g)\nabla s_w\right) = 0\end{aligned} \tag{16}$$

We again multiply by a test function $w \in \mathcal{V}$, integrate by parts, and sum over the elements and edges to obtain:

$$\begin{aligned}\sum_{T\in\mathcal{M}_h} &\int_T \frac{\partial(\phi s_w)}{\partial t} w + \sum_{T\in\mathcal{M}_h}\int_T K\alpha(s_w, s_g)\nabla s_w \cdot \nabla w \\ &- \sum_{e\in\Gamma_h^i\cup\Gamma_{s_1}}\int_e \langle K\alpha(s_w, s_g)\nabla s_w \cdot \mathbf{n}_e\rangle [w] \\ &+\epsilon \sum_{e\in\Gamma_h^i\cup\Gamma_{p_1}}\int_e \langle K\alpha(s_w, s_g)\nabla w \cdot \mathbf{n}_e\rangle [s_w] \\ &+ \sum_{e\in\Gamma_h^i\cup\Gamma_{s_1}}\frac{\sigma}{|e|}\int_e [s_w][w] \\ &- \sum_{T\in\mathcal{M}_h}\int_T \nabla w \cdot \frac{\lambda_w}{\lambda_t}\chi(p_o, s_w, s_g) \\ &+ \sum_{e\in\Gamma_h^i\cup\partial\Omega}\int_e \left(\frac{\lambda_w}{\lambda_t}\right)^* \chi(p_o, s_w, s_g)\cdot \mathbf{n}_e [w] \\ &= \sum_{e\in\Gamma_{s_1}}\int_e \left(\epsilon K\alpha(s_w, s_g)\nabla w \cdot \mathbf{n}_e + \frac{\sigma}{|e|}w\right) s_{w,D}\end{aligned} \tag{17}$$

Here, $(\lambda_w/\lambda_t)^*$ denotes the numerical upwind flux again.

3.3 The light oil saturation equation

We define the auxiliary variables Λ and β:

$$\begin{aligned}\boldsymbol{\Lambda}(p_o, s_w, s_g) &= \mathbf{u}(p_o, s_w, s_g) \\ &\quad + K\lambda_w p'_{cwo}\nabla s_w \\ \beta(s_w, s_g) &= \frac{\lambda_g(\lambda_o + \lambda_w)}{\lambda_t} p'_{cgo}\end{aligned}$$

and rewrite (2) as follows:

$$\begin{aligned}\frac{\partial(\phi s_g)}{\partial t} &+ \nabla \cdot \frac{\lambda_g}{\lambda_t}\Lambda(p_o, s_w, s_g) \\ &- \nabla \cdot \left(K\beta(s_w, s_g)\nabla s_g\right) = 0\end{aligned} \tag{18}$$

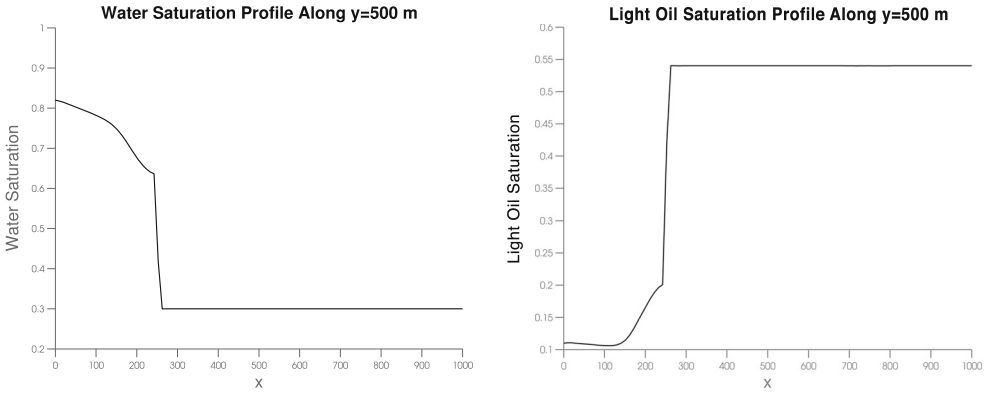

Fig. 6 The saturation profiles along $y = 500$ at 113 days for the example on an inhomogeneous medium using NIPG with $\sigma = 1.0$ and $p = 2$

We again multiply by a test function $z \in \mathcal{V}$ and integrate by parts and sum over the elements and edges to obtain:

$$\begin{aligned}
\sum_{T\in\mathcal{M}_h} & \int_T \frac{\partial(\phi s_{\mathrm{g}})}{\partial t} z + \sum_{T\in\mathcal{M}_h} \int_T K\beta(s_{\mathrm{w}}, s_{\mathrm{g}})\nabla s_{\mathrm{g}} \cdot \nabla z \\
& - \sum_{e\in\Gamma_h^i\cup\Gamma_{s_1}} \int_e \left\langle K\beta(s_{\mathrm{w}}, s_{\mathrm{g}})\nabla s_{\mathrm{g}} \cdot \mathbf{n}_e \right\rangle [z] \\
& + \epsilon \sum_{e\in\Gamma_h^i\cup\Gamma_{p_1}} \int_e \left\langle K\beta(s_{\mathrm{w}}, s_{\mathrm{g}})\nabla z \cdot \mathbf{n}_e \right\rangle [s_{\mathrm{g}}] \\
& + \sum_{e\in\Gamma_h^i\cup\Gamma_{s_1}} \frac{\sigma}{|e|} \int_e [s_{\mathrm{g}}][z] \\
& - \sum_{T\in\mathcal{M}_h} \int_T \nabla w \cdot \frac{\lambda_{\mathrm{g}}}{\lambda_{\mathrm{t}}} \Lambda(p_{\mathrm{o}}, s_{\mathrm{w}}, s_{\mathrm{g}}) \\
& + \sum_{e\in\Gamma_h^i\cup\partial\Omega} \int_e \left(\frac{\lambda_{\mathrm{g}}}{\lambda_{\mathrm{t}}}\right)^* \Lambda(p_{\mathrm{o}}, s_{\mathrm{w}}, s_{\mathrm{g}}) \cdot \mathbf{n}_e [z] \\
= & \sum_{e\in\Gamma_{s_1}} \int_e \left(\epsilon K\beta(s_{\mathrm{w}}, s_{\mathrm{g}})\nabla z \cdot \mathbf{n}_e + \frac{\sigma}{|e|} z\right) s_{\mathrm{g,D}} \qquad (19)
\end{aligned}$$

Here, $(\lambda_{\mathrm{g}}/\lambda_{\mathrm{t}})^*$ denotes the numerical upwind flux again.

4 Fully discrete scheme

For the saturation equations, we discretize the transient term using the backward Euler method. We denote the solutions at the k^{th} time step by $(p_{\mathrm{o}}^k, s_{\mathrm{w}}^k, s_{\mathrm{g}}^k)$. The solutions at time $t = 0$ are denoted by s_{w}^0, s_{g}^0 and computed using L^2 projections on the initial conditions.

For the oil pressure equation, we time lag the saturations, effectively linearizing the source terms and diffusion coefficients. For the water saturation equation, we time lag the coefficients using the values of the heavy oil pressure and light oil saturations, but the equation is kept nonlinear with respect to the water saturation unknown. Similarly, the light oil saturation is kept nonlinear with respect to the light oil saturation unknown, while using the computed values for the oil pressure and water saturation from the previous steps. At each time step, we resolve the nonlinearity using

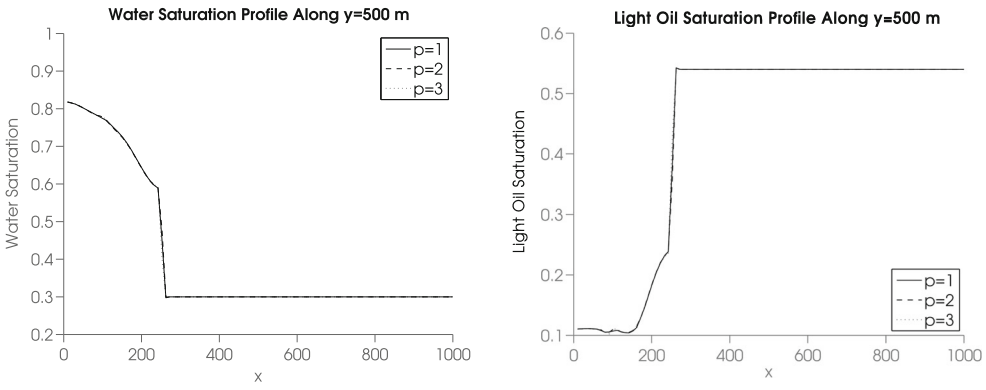

Fig. 7 A comparison of the saturation profiles along $y = 500$ m for $p \in \{1, 2, 3\}$ after 110 days

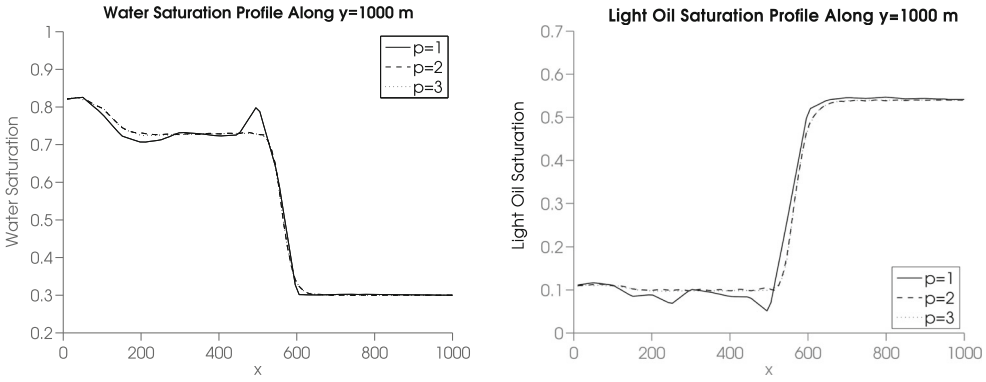

Fig. 8 A comparison of the saturation profiles along $y = 1000$ m for $p \in \{1, 2, 3\}$ after 110 days

Newton's method. The resulting algorithm is called semi-implicit because the system is decoupled but each equation requires the construction of a Jacobian. Given $(p_o^k, s_w^k, s_g^k) \in \mathcal{V} \times \mathcal{V} \times \mathcal{V}$, we seek $(p_o^{k+1}, s_w^{k+1}, s_g^{k+1}) \in \mathcal{V} \times \mathcal{V} \times \mathcal{V}$ such that for all $(v, w, z) \in \mathcal{V} \times \mathcal{V} \times \mathcal{V}$, we have:

$$
\begin{aligned}
\sum_{T\in\mathcal{M}_h} & \int_T K\lambda_t(s_w^k, s_g^k)\nabla p_o^{k+1}\cdot\nabla v \\
& - \sum_{e\in\Gamma_h^i\cup\Gamma_{p_1}} \int_e \langle K\lambda_t(s_w^k, s_g^k)\nabla p_o^{k+1}\cdot\mathbf{n}_e\rangle[v] \\
& + \epsilon \sum_{e\in\Gamma_h^i\cup\Gamma_{p_1}} \int_e \langle K\lambda_t(s_w^k, s_g^k)\nabla v\cdot\mathbf{n}_e\rangle[p_o^{k+1}] \\
& + \sum_{e\in\Gamma_h^i\cup\Gamma_{p_1}} \frac{\sigma}{|e|}\int_e [p_o^{k+1}][v] = \sum_{T\in\mathcal{M}_h}\int_T \nabla v\cdot\zeta^k \\
& - \sum_{e\in\Gamma_h^i\cup\partial\Omega} \int_e \left(\zeta^k\right)^*\cdot\mathbf{n}_e[v] - \sum_{T\in\mathcal{M}_h}\int_T \nabla v\cdot\xi^k \\
& - \sum_{e\in\Gamma_h^i\cup\partial\Omega} \int_e \left(\xi^k\right)^*\cdot\mathbf{n}_e[v] \\
& + \sum_{e\in\Gamma_{p_1}} \int_e \left(\epsilon K\lambda_t(s_w^k, s_g^k)\nabla v\cdot\mathbf{n}_e + \frac{\sigma}{|e|}v\right) p_{o,D}
\end{aligned}
\tag{20}
$$

and

$$
\begin{aligned}
\sum_{T\in\mathcal{M}_h} & \frac{1}{\Delta t} \int_T \phi s_w^{k+1} w \\
& + \sum_{T\in\mathcal{M}_h} \int_T K\alpha(s_w^{k+1}, s_g^k)\nabla s_w^{k+1}\cdot\nabla w \\
& + \sum_{e\in\Gamma_h^i\cup\Gamma_{s_1}} \int_e \left\langle K\alpha(s_w^{k+1}, s_g^k)\nabla s_w^{k+1}\cdot\mathbf{n}_e\right\rangle[w] \\
& + \epsilon \sum_{e\in\Gamma_h^i\cup\Gamma_{s_1}} \int_e \left\langle K\alpha(s_w^{k+1}, s_g^k)\nabla w\cdot\mathbf{n}_e\right\rangle[s_w^{k+1}] \\
& + \sum_{e\in\Gamma_h^i\cup\Gamma_{s_1}} \frac{\sigma}{|e|}\int_e [s_w^{k+1}][w] \\
& - \sum_{T\in\mathcal{M}_h} \int_T \nabla w\cdot\frac{\lambda_w(s_w^{k+1})}{\lambda_t(s_w^{k+1}, s_g^k)} \\
& \times \boldsymbol{\chi}(p_o^{k+1}, s_w^k, s_g^k) \\
& + \sum_{e\in\Gamma_h^i\cup\partial\Omega} \int_e \left(\frac{\lambda_w(s_w^{k+1})}{\lambda_t(s_w^{k+1}, s_g^k)}\right)^* \\
& \times \langle\chi(p_o^{k+1}, s_w^k, s_g^k)\cdot\mathbf{n}_e\rangle[w] \\
= & \sum_{T\in\mathcal{M}_h} \frac{1}{\Delta t}\int_T \phi s_w^k w \\
& + \sum_{e\in\Gamma_{s_1}} \int_e \left(\epsilon K\alpha(s_w^{k+1}, s_g^k)\nabla w\cdot\mathbf{n}_e + \frac{\sigma}{|e|}v\right) s_{w,D}
\end{aligned}
\tag{21}
$$

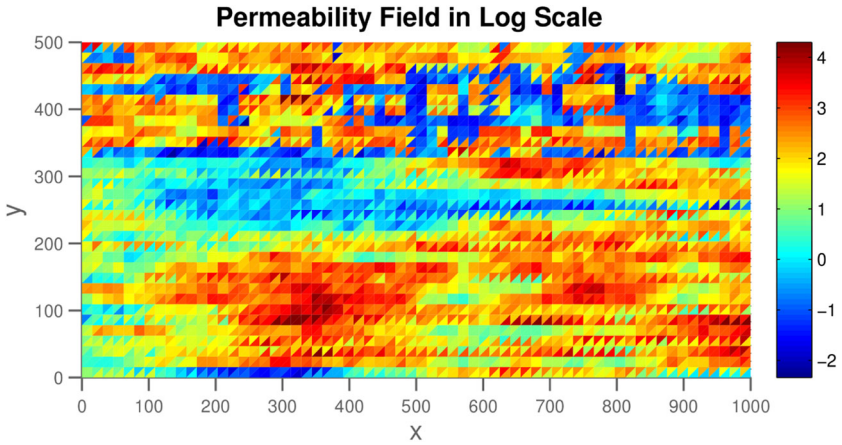

Fig. 9 The permeability field corresponding to $\mathcal{M}_1$ for the h-convergence study

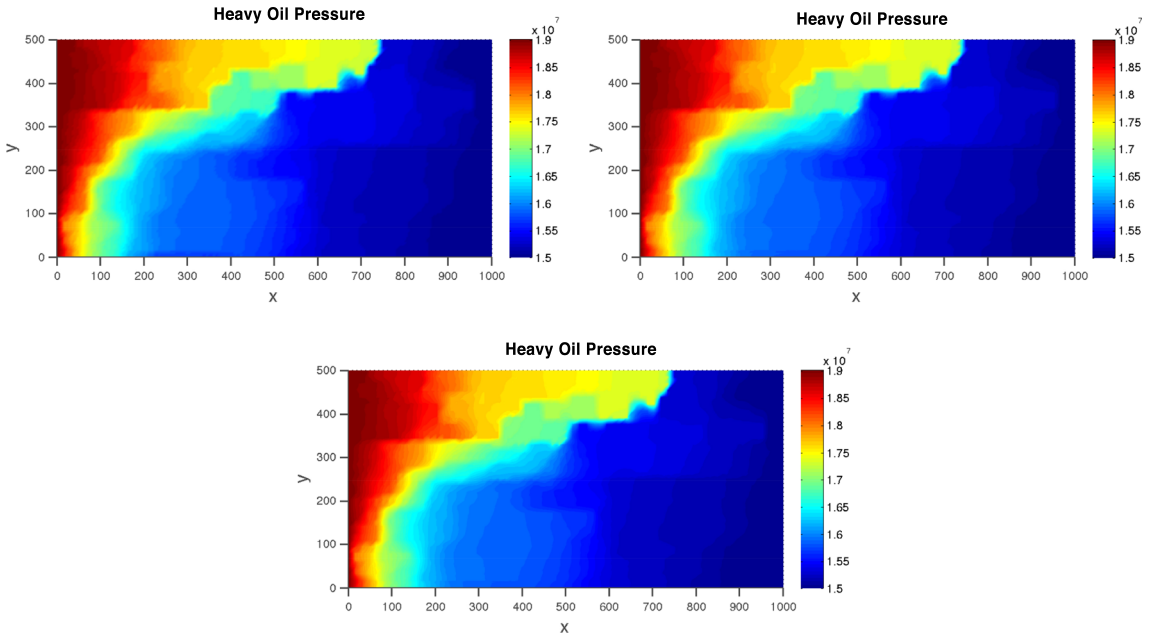

Fig. 10 The two-dimensional pressure contours at 65 days for the convergence study example on $\mathcal{M}_1$ (*top*), $\mathcal{M}_2$ (*middle*), and $\mathcal{M}_3$ (*bottom*) using NIPG with $\sigma = 1.0$ and $p = 2$

and

$$
\begin{aligned}
\sum_{T\in\mathcal{M}_h}\frac{1}{\Delta t}\quad & \int_T \phi s_{\mathrm{g}}^{k+1} z + \sum_{T\in\mathcal{M}_h}\int_T K\beta(s_{\mathrm{w}}^{k+1}, s_{\mathrm{g}}^{k+1})\nabla s_{\mathrm{g}}^{k+1}\cdot\nabla z \\
& + \sum_{e\in\Gamma_h^i\cup\Gamma_{s_1}}\int_e \left\langle K\beta(s_{\mathrm{w}}^{k+1}, s_{\mathrm{g}}^{k+1})\nabla s_{\mathrm{g}}^{k+1}\cdot\mathbf{n}_e\right\rangle [z] \\
& + \sum_{e\in\Gamma_h^i\cup\Gamma_{s_1}}\int_e \left\langle K\beta(s_{\mathrm{w}}^{k+1}, s_{\mathrm{g}}^{k+1})\nabla z\cdot\mathbf{n}_e\right\rangle [s_{\mathrm{g}}^{k+1}] \\
& + \sum_{e\in\Gamma_h^i\cup\Gamma_{s_1}}\frac{\sigma}{|e|}\int_e [s_{\mathrm{g}}^{k+1}][z] \\
& - \sum_{T\in\mathcal{M}_h}\int_T \nabla z\cdot\frac{\lambda_{\mathrm{g}}(s_{\mathrm{g}}^{k+1})}{\lambda_{\mathrm{t}}(s_{\mathrm{w}}^{k+1}, s_{\mathrm{g}}^{k+1})} \\
& \times\mathbf{\Lambda}(p_{\mathrm{o}}^{k+1}, s_{\mathrm{w}}^{k+1}, s_{\mathrm{g}}^{k}) \\
& + \sum_{e\in\Gamma_h^i\cup\partial\Omega}\int_e \left(\frac{\lambda_{\mathrm{g}}(s_{\mathrm{g}}^{k+1})}{\lambda_{\mathrm{t}}(s_{\mathrm{w}}^{k+1}, s_{\mathrm{g}}^{k})}\right)^{*} \\
& \times\langle\Lambda(p_{\mathrm{o}}^{k+1}, s_{\mathrm{w}}^{k+1}, s_{\mathrm{g}}^{k})\cdot\mathbf{n}_e\rangle[z] \\
= & \sum_{T\in\mathcal{M}_h}\frac{1}{\Delta t}\int_T \phi s_{\mathrm{g}}^{k} z \\
& + \sum_{e\in\Gamma_{s_1}}\int_e \left(\epsilon K\beta(s_{\mathrm{w}}^{k+1}, s_{\mathrm{g}}^{k+1})\nabla z\cdot\mathbf{n}_e + \frac{\sigma}{|e|}v\right) s_{\mathrm{g,D}} \qquad (22)
\end{aligned}
$$

Equation 20 is the pressure equation; it is first solved, and the resulting pressure is used as input in the water saturation equation (21). The light oil saturation equation (22) is solved last, with the heavy oil pressure and water saturation at the current time step as input parameters. To recover the heavy oil saturation, we use the closure relation:

$$s_o^{k+1} = 1.0 - s_w^{k+1} - s_g^{k+1}$$

5 Numerical results

5.1 Homogeneous medium

For the first numerical simulation, we consider a square kilometer computational domain $\Omega = [0\text{ m}, 1000\text{ m}]^2$. We take the residual saturations $s_{\mathrm{wr}} = 0$ and $s_{\mathrm{or}} = 0$. We take the following viscosities:

$$\mu_{\mathrm{w}} = 0.0001\ \frac{\mathrm{kg}}{\mathrm{m}\cdot\mathrm{s}} \quad \mu_{\mathrm{o}} = 0.0005\ \frac{\mathrm{kg}}{\mathrm{m}\cdot\mathrm{s}} \quad \mu_{\mathrm{g}} = 0.00001\ \frac{\mathrm{kg}}{\mathrm{m}\cdot\mathrm{s}}$$

We consider a uniform mesh of 2048 triangular elements with $K = 10^{-10}\ \mathrm{m}^2$ and $\phi = 0.2$ for all $(x, y) \in \Omega$. We define the left and right boundaries to be the Dirichlet boundaries as follows:

$$
\begin{aligned}
&p_{\mathrm{o}}(x = 0\text{ m}) = 19.0\text{ MPa} && p_{\mathrm{o}}(x = 1000\text{ m}) = 15.0\text{ MPa}\\
&s_{\mathrm{w}}(x = 0\text{ m}) = 0.82 && s_{\mathrm{w}}(x = 1000\text{ m}) = 0.30\\
&s_{\mathrm{g}}(x = 0\text{ m}) = 0.11 && s_{\mathrm{g}}(x = 1000\text{ m}) = 0.54
\end{aligned}
$$

We first use the NIPG method with $\sigma = 1.0$. We take $p \in \{1, 2, 3, 4\}$ and a time step of $\Delta t = 0.1$ days. The saturation profiles after 100 days are given in Fig. 1.

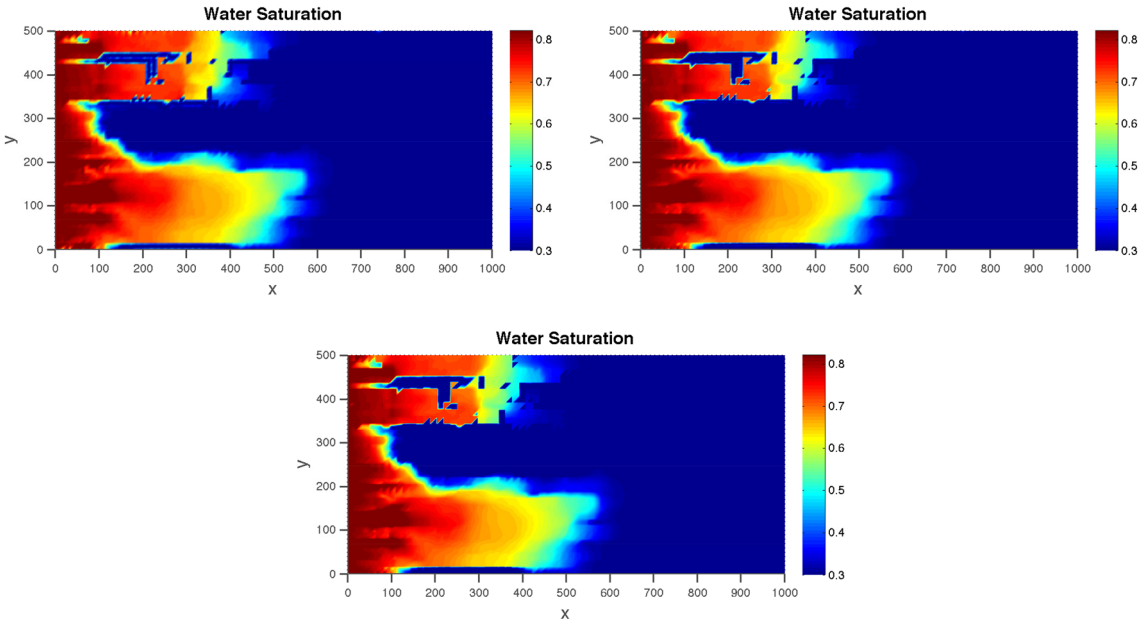

Fig. 11 The two-dimensional water saturation contours at 65 days for the convergence study example on $\mathcal{M}_1$ (*top*), $\mathcal{M}_2$ (*middle*), and $\mathcal{M}_3$ (*bottom*) using NIPG with $\sigma = 1.0$ and $p = 2$

We see that quadratic basis functions offer a significant increase in accuracy over linear basis functions. Cubic and quartic basis functions offer a further, but less noticeable, increase in accuracy.

5.2 Inhomogeneous medium

For the second numerical simulation, we use the same parameters as in the first simulation but imbed a large

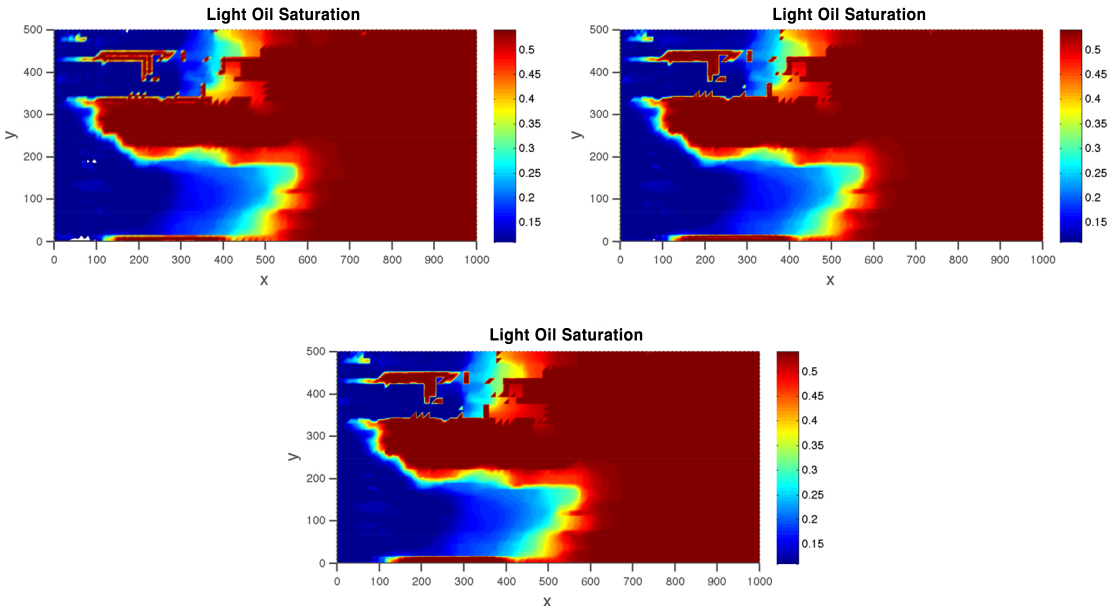

Fig. 12 The two-dimensional light oil saturation contours at 65 days for the convergence study example on $\mathcal{M}_1$ (*top*), $\mathcal{M}_2$ (*middle*), and $\mathcal{M}_3$ (*bottom*) using NIPG with $\sigma = 1.0$ and $p = 2$

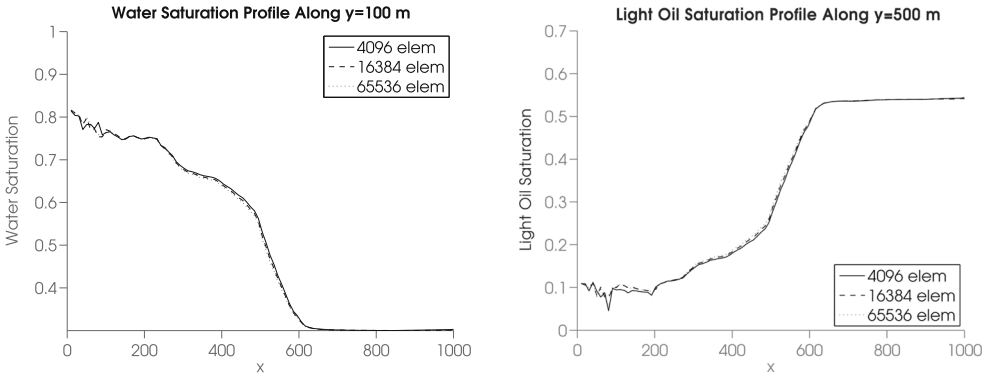

Fig. 13 The one-dimensional saturation contours at 65 days for the convergence study example on $\mathcal{M}_1$ (*solid line*), $\mathcal{M}_2$ (*dashed line*), and $\mathcal{M}_3$ (*dotted line*) using NIPG with $\sigma = 1.0$ and $p = 2$

impermeable region $\Omega_K \subseteq \Omega$ where $K = 10^{-13}$ m^2. We take $\Omega_K = [250\text{ m}, 750\text{ m}]^2$.

We consider a mesh of 9800 triangular elements that is refined greatly in a small region around $\partial\Omega_K$ as shown in Fig. 2. We use the NIPG method with $\sigma = 1.0$. We take a time step of $\Delta t = 0.1$ days. The two-dimensional pressure and saturation contours at 113 and 226 days are given in Figs. 3 and 4 for the piecewise quadratic approximations ($p = 2$). The pressure and saturation profiles along the line $y = 500$ m are given in Figs. 5 and 6.

We see that the scheme is able to accurately capture the impermeable regions. Furthermore, the solution at the boundary of Ω_K remains sharp and well-pronounced; there is very little overshoot and undershoot and no slope limiters are required. Unlike explicit schemes that require a constraint on the time step for stability, the semi-implicit scheme allows us to take a relatively large time step and still obtain a stable solution. Newton's method always converges within 2 to 3 iterations using a tolerance of 10^{-11} for this example.

Next, we consider varying the degree of the polynomial basis functions. We take $\sigma = 1.0$, $\Delta t = 1.0$ days, and $p \in \{1, 2, 3\}$. The saturation profiles along the midline $y = 500$ m after 110 days are given in Fig. 7. The saturation profiles along the upper edge of the domain after 110 days are given in Fig. 8. We see that although each basis is able to effectively capture the behavior of the region of lower permeability in the center of the domain, the behavior in

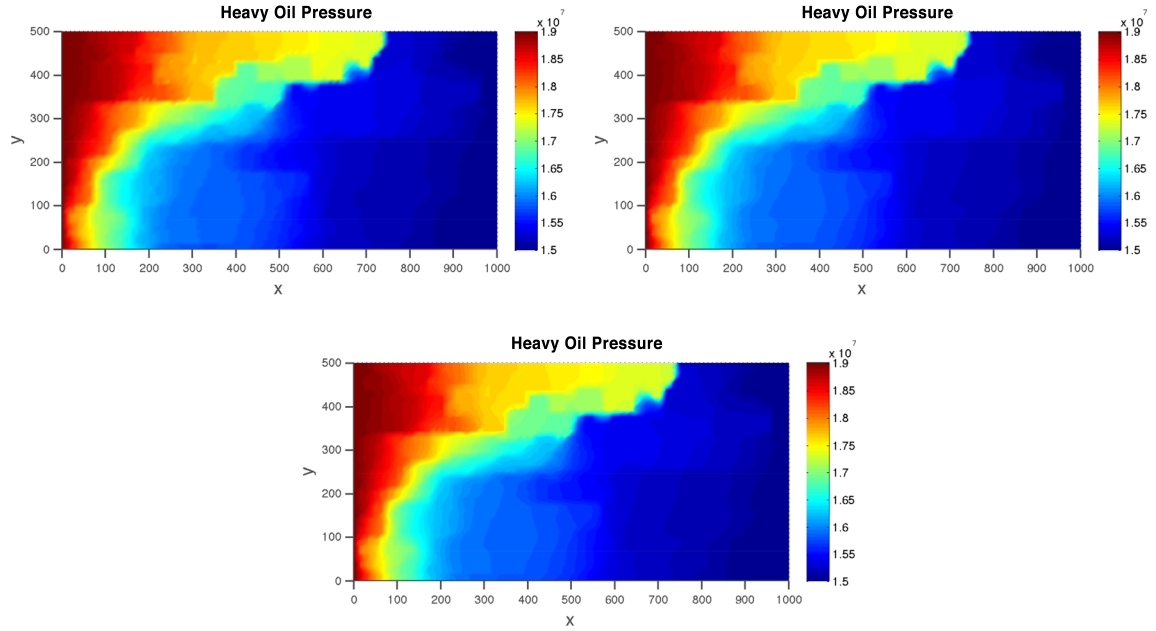

Fig. 14 The two-dimensional pressure contours at 65 days for the convergence study example on $\mathcal{M}_2$ using NIPG with $p = 1$ (*top*), $p = 2$ (*middle*), and $p = 3$ (*bottom*) and $\sigma = 1.0$

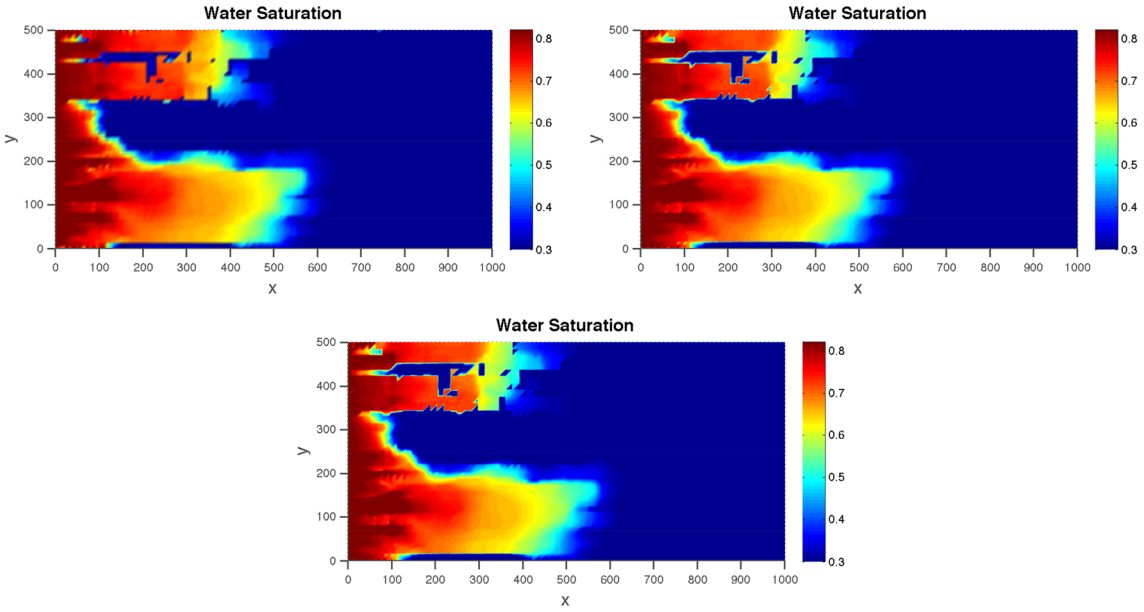

Fig. 15 The two-dimensional water saturation contours at 65 days for the convergence study example on $\mathcal{M}_2$ using NIPG with $p = 1$ (*top*), $p = 2$ (*middle*), and $p = 3$ (*bottom*) and $\sigma = 1.0$

the vicinity of $\partial\Omega$ varies considerably. For $p = 1$, spurious oscillations and significant overshoot and undershoot can be seen. As we increase the order of the basis to $p = 2, 3$, we see a much smoother solution.

5.3 Convergence study

Since there is no theoretical proof of convergence for the scheme (20)–(22), we numerically test the numerical

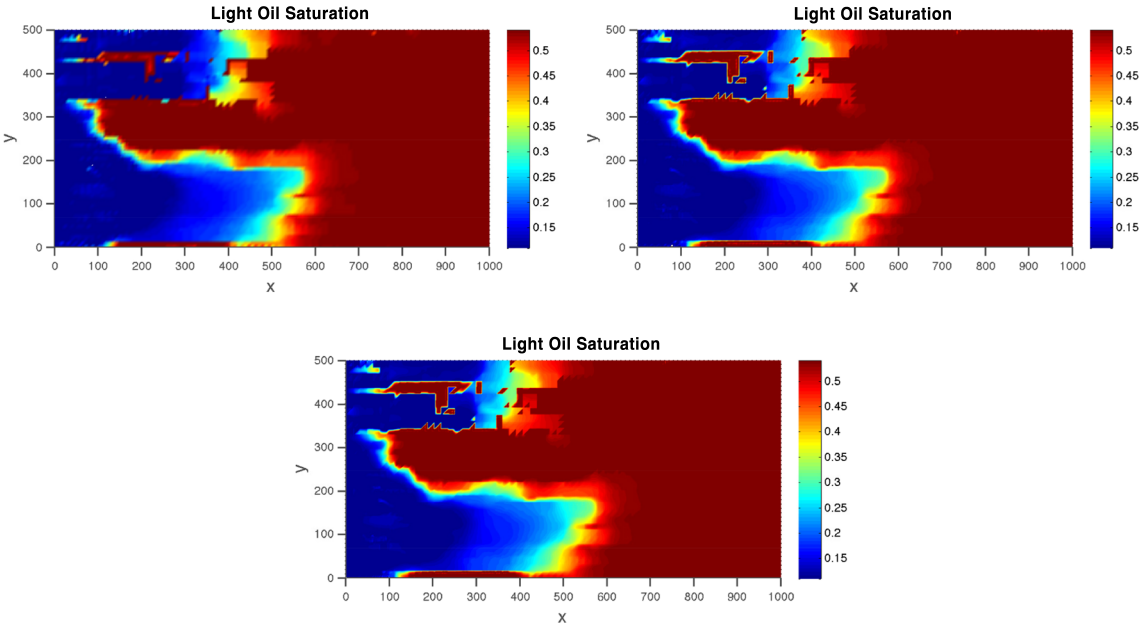

Fig. 16 The two-dimensional light oil saturation contours at 65 days for the convergence study example on $\mathcal{M}_2$ using NIPG with $p = 1$ (*top*), $p = 2$ (*middle*), and $p = 3$ (*bottom*) and $\sigma = 1.0$

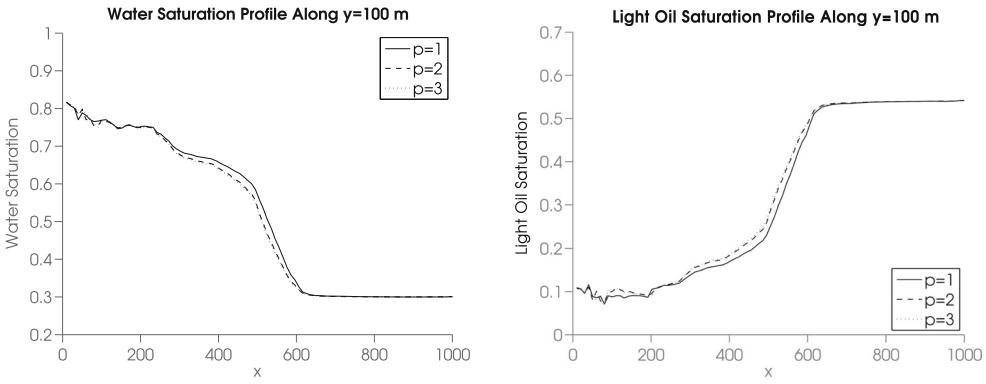

Fig. 17 The one-dimensional saturation contours at 65 days for the convergence study example on $\mathcal{M}_2$ using NIPG with $p = 1$ (*solid line*), $p = 2$ (*dashed line*), and $p = 3$ (*dotted line*) and $\sigma = 1.0$

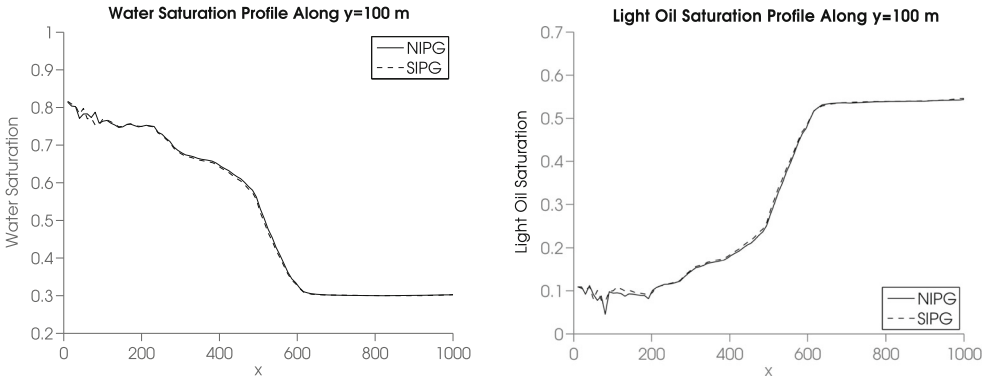

Fig. 18 The one-dimensional saturation contours at 65 days for the convergence study example on $\mathcal{M}_2$ using NIPG (*solid line*) and SIPG (*dashed line*) with $p = 2$ and $\sigma = 1.0$

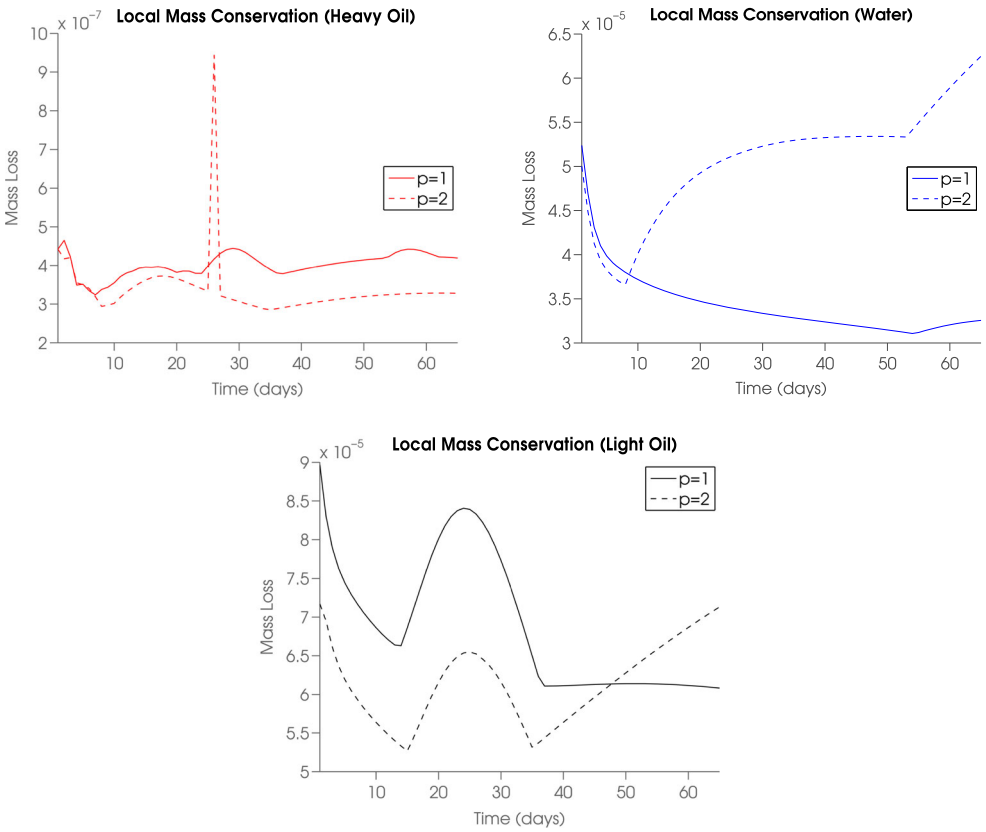

Fig. 19 The mass loss for the heavy oil, water, and light oil saturations for the SPE 10 benchmark problem using $p \in \{1, 2\}$ and $\Delta t = 1.0$ day

Table 1 The maximum mass loss over all time steps and mesh elements for the phase saturations after 65 days using NIPG with $p \in \{1, 2\}$ and $\sigma = 1.0$

	$p = 1$	$p = 2$
$\max_k \max_T E^k_{s_o,T}$	4.4698×10^{-7}	9.4353×10^{-7}
$\max_k \max_T E^k_{s_w,T}$	5.2374×10^{-5}	6.2000×10^{-5}
$\max_k \max_T E^k_{s_g,T}$	8.9670×10^{-5}	7.2000×10^{-5}

convergence of the scheme by (i) varying the mesh size (also called h-refinement) and (ii) varying the degree of the polynomial basis functions (also called p-refinement). We choose small time steps so that the dominant error is from the spatial discretization. We expect that as we refine the mesh uniformly successively, the numerical error decreases toward zero. This means that the numerical solutions converge to the exact solution. For an exact manufactured solution, we can recover the optimal rates of convergence. In the examples in this section, the exact solution is not known as the input coefficients (such as permeability) vary greatly in space.

We consider a 120×54 cell cut of the 30th vertical layer of the permeability field from the data in [11]. We fix the porosity to be 0.20 throughout the domain. We first consider the effect of h-refinement on the solution. We consider three partitions of the computational domain $\Omega = [0\text{ m}, 1000\text{ m}] \times [0\text{ m}, 500\text{ m}]$: $\mathcal{M}_1$, $\mathcal{M}_2$, and $\mathcal{M}_3$ consisting of 4096, 16,384, and 65,536 uniform triangular elements, respectively. The permeability field is upscaled to adhere to the coarsest mesh, $\mathcal{M}_1$, as shown in Fig. 9. The permeability varies over six orders of magnitude.

The two-dimensional pressure and saturation contours after 65 days are given in Figs. 10, 11, and 12. The one-dimensional saturation profiles along $y = 100$ m are given in Fig. 13. We see that there is relatively little variance among the solutions on each mesh.

Next, we consider the effect of p-refinement on the solution. Namely, we fix the mesh to contain 16,384 uniform triangular elements as in $\mathcal{M}_2$ and take $p \in \{1, 2, 3\}$. We expect the numerical errors to decrease as we increase the polynomial degree.

The two-dimensional pressure and saturation contours after 65 days are given in Figs. 14, 15, and 16. The one-dimensional saturation profiles along $y = 100$ m are given in Fig. 17. We see again that there is relatively little variance among the solutions. However, it should be noted that the solution for $p = 1$ varies more than between $p = 2$ and $p = 3$.

Lastly, we consider the same problem on $\mathcal{M}_2$ with $p = 2$. We compare the solutions using NIPG and SIPG with $\sigma = 1.0$ after 65 days. The saturation profiles are given in Fig. 18. We see that there is little difference between the solutions regardless of the variant of the DG method that is used.

5.4 Local mass conservation

We now consider the local mass balance in our numerical scheme. The system (1)–(4) is derived from the mass balance equations for each phase:

$$\frac{\partial(\phi s_i)}{\partial t} + \nabla \cdot \mathbf{u}_i = 0, \quad \mathbf{u}_i = -K\lambda_i \nabla p_i, i = g, o, w.$$

where the phase velocities are denoted by $\mathbf{u}_i$. At the discrete level, the mass loss for the phases on element T at the k^{th} time step are given by:

$$E^k_{s_o,T} = \tfrac{1}{\Delta t}\int_T \phi\left(s^k_o - s^{k-1}_o\right) + \int_{\partial T}\langle \mathbf{u}^k_o \cdot \mathbf{n}_T\rangle \quad (23)$$

$$E^k_{s_w,T} = \tfrac{1}{\Delta t}\int_T \phi\left(s^k_w - s^{k-1}_w\right) + \int_{\partial T}\langle \mathbf{u}^k_w \cdot \mathbf{n}_T\rangle \quad (24)$$

$$E^k_{s_g,T} = \tfrac{1}{\Delta t}\int_T \phi\left(s^k_g - s^{k-1}_g\right) + \int_{\partial T}\langle \mathbf{u}^k_g \cdot \mathbf{n}_T\rangle \quad (25)$$

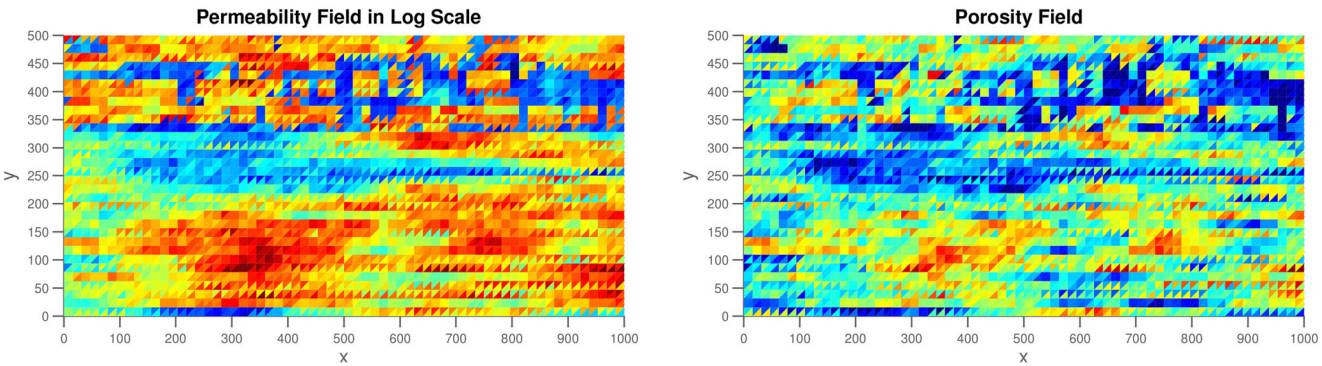

Fig. 20 The permeability field and porosity field for the first SPE 10 benchmark example

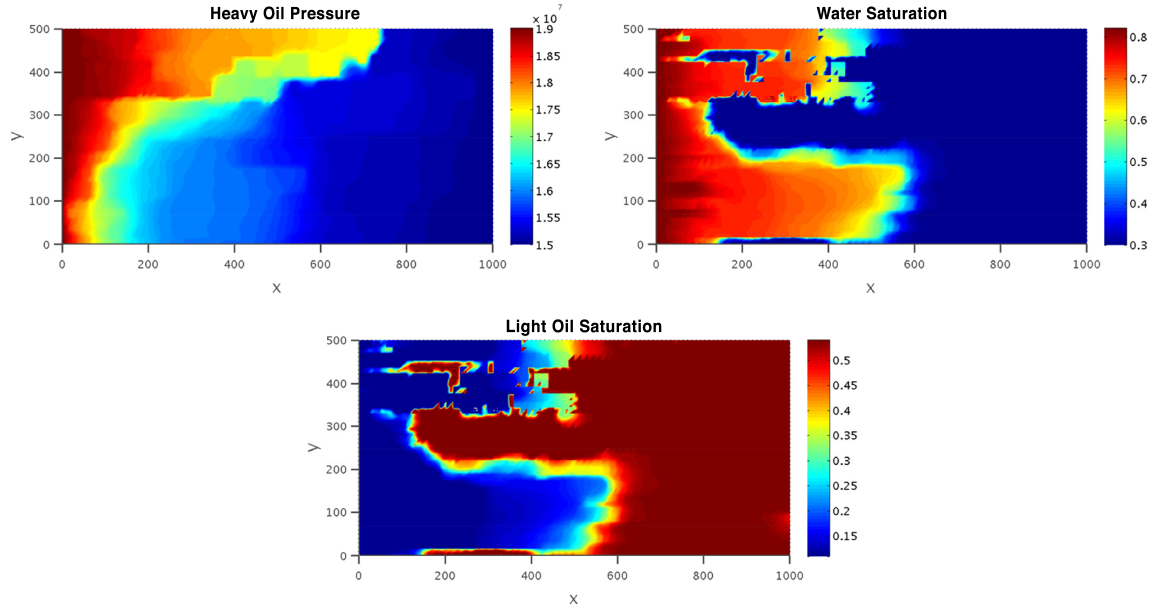

Fig. 21 The two-dimensional pressure and saturation contours at 102 days for the first SPE 10 example using piecewise cubic approximations

where the individual phase velocities are computed from the primary unknowns by:

$$\mathbf{u}_{\mathrm{o}}^{k} = -K\lambda_{\mathrm{o}}(s_{\mathrm{w}}^{k}, s_{\mathrm{g}}^{k})\nabla p_{\mathrm{o}}^{k} \tag{26}$$

$$\mathbf{u}_{\mathrm{w}}^{k} = -K\lambda_{\mathrm{w}}(s_{\mathrm{w}}^{k}) \times \left(\nabla p_{\mathrm{o}}^{k} - p'_{\mathrm{cwo}}(s_{\mathrm{w}}^{k})\nabla s_{\mathrm{w}}^{k}\right) \tag{27}$$

$$\mathbf{u}_{\mathrm{g}}^{k} = -K\lambda_{\mathrm{g}}(s_{\mathrm{g}}^{k}) \times \left(\nabla p_{\mathrm{o}}^{k} - p'_{\mathrm{cgo}}(s_{\mathrm{g}}^{k})\nabla s_{\mathrm{g}}^{k}\right) \tag{28}$$

We remark that because our scheme is based on the DG discretization of a different system of PDEs (1)–(4), our numerical solutions satisfy a different system of discrete mass balance equations. For instance, choosing a test function w to be equal to one on the mesh element T and zero elsewhere in (21) yields:

$$\frac{1}{\Delta t}\int_T \phi\left(s_{\mathrm{w}}^{k} - s_{\mathrm{w}}^{k-1}\right) + \int_{\partial T}\langle K\alpha(s_w^{k+1}, s_g^{k})\nabla s_w^{k+1}\cdot\mathbf{n}_T\rangle + \sum_{e\in\partial T}\frac{\sigma}{|e|}\int_e (s_w^{k}|_T - s_w^{k}|_{T_e}) + \int_{\partial T}(\frac{\lambda_w}{\lambda_t})^{*}\langle\chi\cdot\mathbf{n}_T\rangle = 0$$

The notation T_e is for the mesh element that shares the face e with the element T, and the unit vector $\mathbf{n}_T$ is the outward normal to T. A similar equation for the light oil saturation can be obtained from Eq. 22. We compute the mass loss for the simulations given in Section 5.3 for the choice

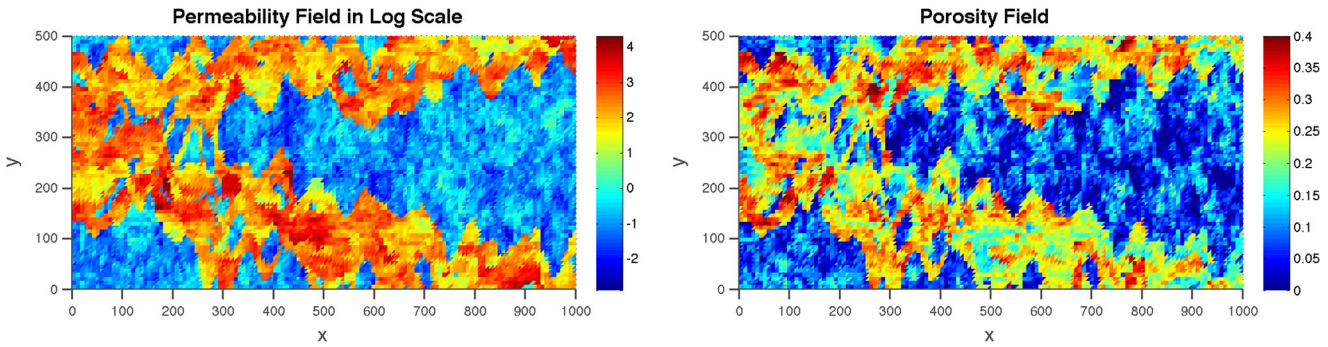

Fig. 22 The permeability field and porosity field for the second SPE 10 benchmark example

of $\Delta t = 1.0$ day. The final time is $t_s = 65.0$ days. The maximum mass loss at each time step, over all mesh elements, is plotted in Fig. 19 for piecewise linear and quadratic solutions. We do not expect the mass loss to be zero but we observe that the values are very small. They are of the order of 10^{-5} for the water and light oil saturations, and of the order of 10^{-7} for the oil saturation. The maximum mass loss for each phase over all mesh elements and time steps is given in Table 1.

5.5 Heterogeneous porosity and permeability

Next, we test the scheme using input data from the SPE 10 benchmark problem [11]. Namely, we consider two-dimensional slices of the provided three-dimensional permeability and porosity fields. There are regions in the domain for which the porosity degenerates.

For the first test, we take a 120×54 cell cut of the 30th vertical layer of the permeability field and porosity field. A visualization of the permeability and porosity fields is given in Fig. 20. The upper portion of this field represents a Tarbert formation while the lower portion represents a fluvial Upper Ness region. The Tarbert formation has more discontinuous geological features than the Upper Ness. The porosity field is also piecewise discontinuous and varies from 0 to 46.7 %. We consider the computational domain $\Omega = [0\ \text{m}, 1000\ \text{m}] \times [0\ \text{m}, 500\ \text{m}]$ and partition the domain into a uniform mesh of 16,384 triangular elements. We point out that the porosity is zero for 208 triangles. We use the NIPG method with $\sigma = 1.0$ and $p = 3$. A time step of $\Delta t = 0.1$ days is used.

The two-dimensional pressure and saturation contours after 102 days are given in Fig. 21. We see that the scheme is able to accurately capture a highly varying permeability field across six orders of magnitude. The saturation contours clearly show the phase displacement is more homogeneous in the bottom region than in the Tarbet formation. Newton's method converges in 3 to 5 iterations with a tolerance of 10^{-11}. We find that using a sequential semi-implicit solution method allows us to take relatively large time steps while still maintaining stability.

For the second test, we take a 220×60 cell cut of the 45th horizontal layer of the permeability and porosity fields. That layer exhibits different geological features than the one for the first test. The domain contains trends, i.e., regions with larger permeability and porosity values, which can be associated to fracture-like features. Visualizations of the permeability and porosity fields are given in Fig. 22. The porosity field is also piecewise discontinuous and varies from 0 to 40 %.

We again consider the computational domain $\Omega = [0\ \text{m}, 1000\ \text{m}] \times [0\ \text{m}, 500\ \text{m}]$ and partition the domain into a uniform mesh of 16,384 triangular elements. For this test case, 640 elements have zero porosity and they are grouped together in the geological features. We use the NIPG method with $\sigma = 1.0$ and $p = 2$. A time step of $\Delta t = 0.1$ days

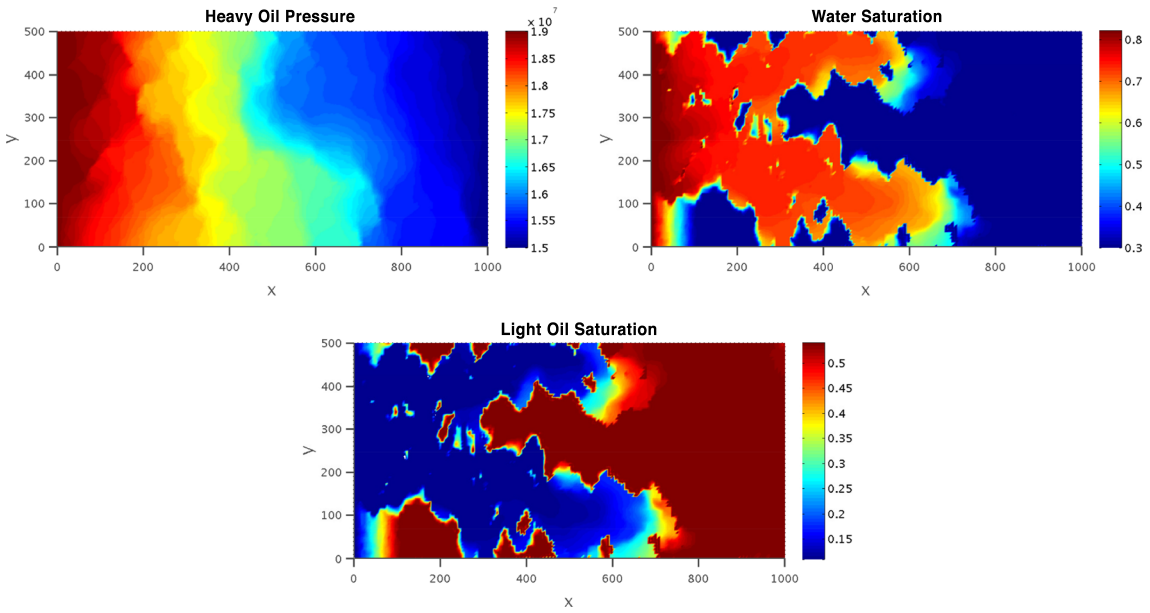

Fig. 23 The two-dimensional pressure and saturation contours at 150 days for the second SPE 10 example using piecewise quadratic approximations

is used. The number of Newton iterations for convergence is initially equal to 6, and then it decreases to 3. The two-dimensional pressure and saturation contours after 150 days are given in Fig. 23.

These numerical results show robustness of the semi-implicit scheme of second and third order, for highly varying permeability and porosity fields. Because of the discontinuous approximations, the numerical method easily handles degenerate porosity fields.

6 Conclusions

In this work, we show the potential of using polynomial approximation of degree up to four for solving an incompressible three-phase flow problem in heterogeneous media. We observe that (i) the numerical mass errors are negligible; (ii) the semi-implicit algorithm stabilizes the solution enough that no slope limiters are required; and (iii) the method converges as the polynomial degree increases even for cases of highly varying discontinuous permeability and porosity fields. In a future work, we would investigate the black-oil problem, which is a three-phase flow with mass transfer between the phases.

References

1. Abreu, E., Douglas, J., Furtado, F., Marchesin, D., Pereira, F.: Three-phase immiscible displacement in heterogeneous petroleum reservoirs. Math. Comput. Simul. **73**(1), 2–20 (2006)
2. Aziz, K., Settari, A.: Petroleum Reservoir Simulation. Applied Science Publishers (1979)
3. Baker, L.: Three-phase relative permeability correlations. Society of Petroleum Engineers (1988). SPE-17369-M
4. Bastian, P.: A fully-coupled discontinuous Galerkin method for two-phase flow in porous media with discontinuous capillary pressure. Comput. Geosci. **18**, 779–796 (2014)
5. Bastian, P., Lang, S.: Couplex benchmark computations obtained with the software toolbox ug. Comput. Geosci. **8**(2), 125–147 (2004)
6. Bentsen, R.G., Anli, J.: A new displacement capillary pressure model. J. Can. Pet. Technol. **15**(3), 75–79 (1976)
7. Berre, I., Dahle, H., Karlson, K., Nordhaug, H.: A streamline front tracking method for two- and three-phase flow including capillary forces. In: Proceedings of an AMS-IMS-SIAM, Joint Summer Research Conference on Fluid Flow and Transport in Porous Media: Mathematical and Numerical Treatment, vol. 295, pp. 49–61 (2002)
8. Brooks, R., Corey, A.: Hydraulic properties of porous media. Hydrol. Pap **3**, 26–28 (1964)
9. Chen, Z., Ewing, R.E.: Comparison of various formulations of three-phase flow in porous media. J. Comput. Phys. **132**(2), 362–373 (1997)
10. Chen, Z., Huan, G., Ma, Y.: Computational Methods for Multiphase Flows in Porous Media. Society for Industrial and Applied Mathematics (SIAM), Philadelphia (2006)
11. Christie, M., Blunt, M.: Tenth SPE comparative solution project: A comparison of upscaling techniques. SPE Res. Simul. Symp. **4**, 308–317 (2001)
12. Dong, J.: A high order method for three phase flow in homogeneous porous media. SIURO **7**, 74–88 (2014)
13. Epshteyn, Y., Rivière, B.: Fully implicit discontinuous finite element methods for two-phase flow. Appl. Numer. Math. **57**, 383–401 (2007)
14. Ern, A., Mozolevski, I.: Discontinuous Galerkin method for two-component liquid gas porous media flows. Comput. Geosci. **16**, 677–690 (2012)
15. Ern, A., Mozolevski, I., Schuh, L.: Discontinuous Galerkin approximation of two-phase flows in heterogeneous porous media with discontinuous capillary pressures. Comput. Methods Appl. Mech. Eng. **199**, 1491–1501 (2010)
16. Klieber, W., Rivière, B.: Adaptive simulations of two-phase flow by discontinuous galerkin methods. Comput. Methods Appl. Mech. Eng. **196**(1), 404–419 (2006)
17. Li, J., Rivière, B.: Numerical solutions of the incompressible miscible displacement equations in heterogeneous media. Comput. Methods Appl. Mech. Eng. **292**, 107–121 (2015)
18. Lu, Q., Peszynska, M., Wheeler, M.: A parallel multi-block black-oil model in multi-model implementation. Soc. Pet. Eng. **7**, 278–287 (2002). SPE 79535
19. Natvig, J.R., Lie, K.A.: Fast computation of multiphase flow in porous media by implicit discontinuous galerkin schemes with optimal ordering of elements. J. Comput. Phys. **227**(24), 10,108–10,124 (2008)
20. Rankin, R., Rivière, B.: A high order method for solving the black-oil problem in porous media. Adv. Water Resour. **78**, 126–144 (2015)
21. Rivière, B.: Discontinuous Galerkin methods for solving elliptic and parabolic equations: Theory and implementation. Soc. Ind. Appl. Math. (2008)
22. Trangenstein, J.A., Bell, J.B.: Mathematical structure of the black-oil model for petroleum reservoir simulation. SIAM J. Appl. Math. **49**(3), 749–789 (1989)